

***Polar Direct Drive Designs for the Laser Megajoule***

**Audrey Kohlman**

Churchville-Chili Senior High School

Churchville, New York

Advisor: Dr. R. Stephen Craxton

**Laboratory for Laser Energetics**

University of Rochester

Rochester, New York

May 2023

## 1. Abstract

The Laser Megajoule (LMJ) is an under-construction French laser facility that is configured for indirect drive implosions. This configuration includes two rings of quads in each hemisphere; these rings are positioned at either  $33.2^\circ$  or  $49.0^\circ$  from the vertical axis. There are four beams in a quad and ten quads within each ring, giving a total of 160 beams. Following a proposal to perform direct drive implosions on the LMJ, simulations using the program *Sage* were run assuming a  $1000\ \mu\text{m}$  radius target; beams were repointed in the theta (longitudinal) and phi (latitudinal) directions and quads were defocused. When user experiments begin in 2024, only half of the beams will be available. Repointing in the phi direction was essential for compensating for the missing beams when simulating the initial experiments. These simulations achieved implosions with low velocity nonuniformities of approximately 2% rms. Simulations of the LMJ at full capacity resulted in even lower nonuniformities of below 1% rms. This demonstration of the feasibility of direct drive on the LMJ is expected to be applicable to a variety of experiments.

## 2. Introduction

Nuclear fusion is a reaction in which atomic nuclei merge together to create different, and typically heavier, nuclei. The energy released by this reaction could one day provide a clean source of energy to the world; therefore, different methods of attaining it have been explored. One such method is inertial confinement fusion (ICF), in which a target comprised of a solid exterior and gaseous interior is required to be the object of laser compression. This target is filled with fuel composed of deuterium-tritium (DT), which is typically a cryogenic layer of solid DT inside the exterior shell together with some DT gas in the interior. The target is compressed so intensely that it reaches temperatures and pressures comparable to those found in the center of stars. The DT fuses together when the target reaches peak compression. Furthermore, fusion takes place during the short period before the target disassembles [1].

There are two means of performing laser-driven ICF: direct drive and indirect drive. Direct drive [Fig. 1a] involves uniformly aiming beams from all directions at the center of the target. Indirect drive [Fig. 1b] involves placing a target within a cylindrical container made of a substance with a high atomic number; this container is known as a hohlraum. Beams are shot through openings on the ends of the hohlraum. After absorbing the beams, the hohlraum irradiates the target with x rays, allowing for a more uniform implosion of the target than what direct drive typically permits. However, direct drive provides a much higher absorption percentage into the target than indirect drive.

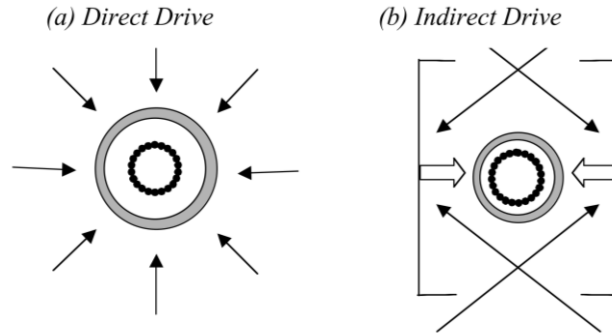


*Figure 1. Two methods of laser fusion. (a) In direct drive, the laser beams (represented by arrows) encompass the target and directly strike it. (b) In indirect drive, the beams come in through opposite ends of a cylindrical container known as a hohlraum, striking its walls which irradiate the target with x-rays. (From Ref. 2)*

Specifically, the U.S. National Ignition Facility (NIF), a 192 beam laser facility, is configured for indirect drive. The beam ports on the NIF are arranged into four rings in each of the upper and lower hemispheres of the target chamber [Fig. 2a]. Rings are composed of quads, which are groups of 4 beam ports. These rings are at 23.5°, 30.0°, 44.5°, and 50.0° from the vertical, respectively. The indirect drive configuration necessitates that these rings are at a large angle from the equator so they may enter the openings of the hohlraum. In contrast, the rings would be more evenly dispersed throughout a chamber configured for direct drive. Using an indirect drive beam configuration for a direct drive implosion would cause high levels of nonuniformity [Fig. 2b]. The poles of the target receive too much energy from the beams and flatten: almost like a pancake. However, this effect can be countered if some of the beams are repointed towards the equator of the target [Fig. 2c]. Previous designs prove the viability of direct drive designs on the NIF.

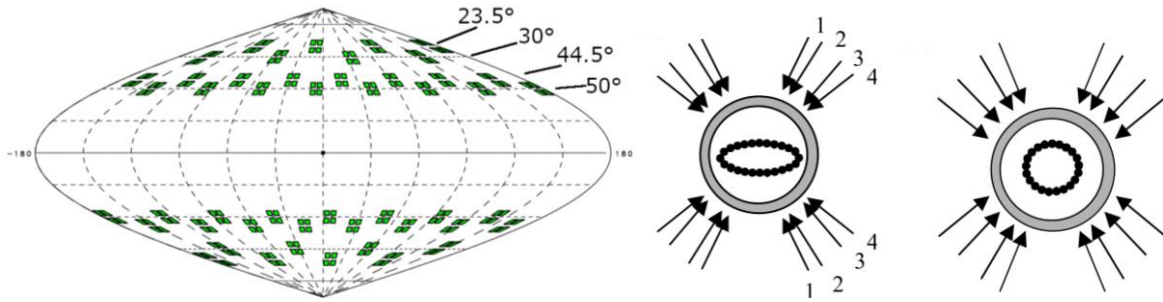


Figure 2. (a) The target chamber of the NIF with its indirect drive configuration. Each small green square represents a laser beam. (From Ref. 3) (b) The resulting implosion of the target with the indirect drive configuration of the NIF. The outer grey circle represents the target before beams are fired while the inner black circle represents the target after the beams have struck it. (c) The resulting implosion of the target when the NIF's beam configuration is adjusted for direct drive. The arrows representing the laser beams spread out towards the equator when these adjustments are made. This increases the amount of energy directed towards the equator and decreases the amount at the poles. The resulting implosion is uniform. (From Ref. 2)

Similarly, the Laser MegaJoule (LMJ) is another laser facility with an initially indirect drive beam configuration that has the potential to permit direct drive experiments. The LMJ has 160 beams that are arranged into two rings in each hemisphere [Fig. 3]; the rings are at angles of 33.2° (Upper Ring) and 49.0° (Lower Ring) from the vertical in the top hemisphere; these angles are reflected onto the bottom hemisphere. Like the NIF, the LMJ's rings are distanced far from the equator in order to facilitate indirect drive experimentation. However, the LMJ has four less rings than the NIF, making it more challenging to develop an apt beam configuration for direct drive. To further exacerbate the issue, only half of the beams will be available for experimentation in 2024. In order to implement direct drive, beams need to be repointed and defocused in a way that allows for the most uniform implosion. Each beam's aimpoint can be moved in the  $\varphi$  (longitude) and  $\theta$  (latitude) directions [Fig. 3].

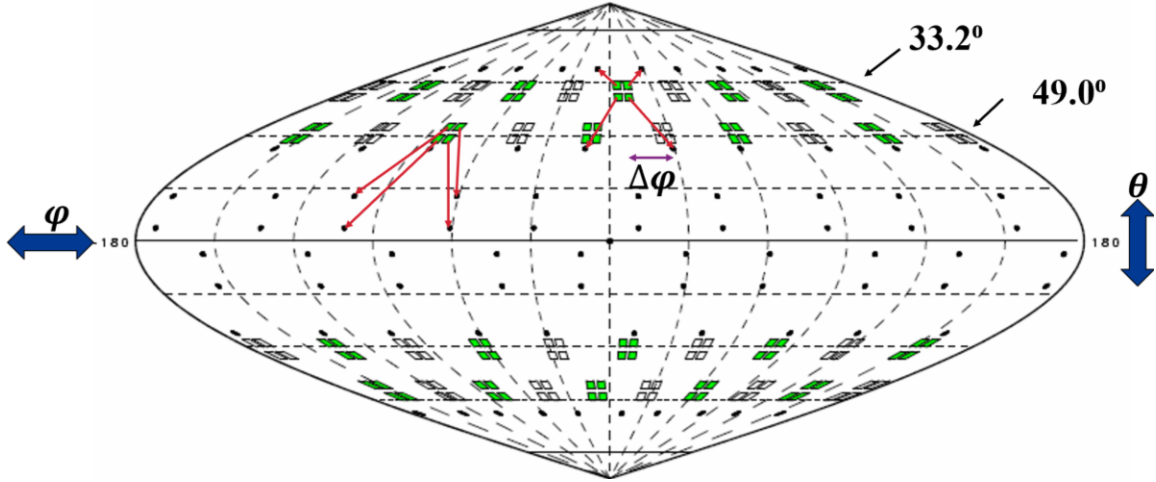


Figure 3. The target chamber for the LMJ in 2024, with beam pointings optimized for direct drive. The LMJ has 40 quads arranged into 4 rings. Green quads are active, while uncolored quads are not. The black dots indicate where the beams will strike the target, or aimpoints. The red arrows show which beam port connects to which aimpoint. The purple arrow represents the change in  $\varphi$ , the left end being the position of the quad center, and the right end being the aimpoint. [Run 1056]

Norreys et al. proposed an experiment to perform direct drive on the LMJ using a 1000  $\mu\text{m}$  radius target, with a carbon-deuterium (CD) shell, followed by a layer of CD foam, which encapsulates the deuterium gas within the target [Fig. 4a] [4]. Notably, deuterium gas is being used in this experiment instead of DT gas, even though DT produces more fusion reactions. This is because tritium is radioactive, making it difficult to handle. Moreover, using deuterium gas allows the implosion dynamics to be studied. The laser pulse is displayed in Figure 4b, with a total energy of 244 kJ. In the present work, the laser pulse shape and the target parameters (75  $\mu\text{m}$  of foam at 0.253  $\text{g}/\text{cm}^3$  followed by a shell thickness of 17.5  $\mu\text{m}$  at 1.04  $\text{g}/\text{cm}^3$  with an outer radius of 997.5  $\mu\text{m}$ ) were taken from Ref. 5, with the minor difference that CH was modeled rather than CD.

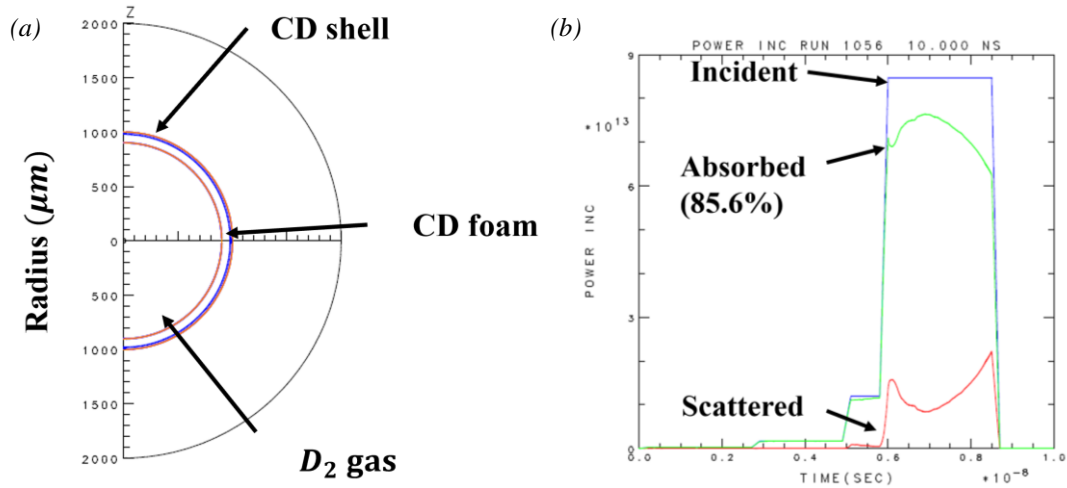
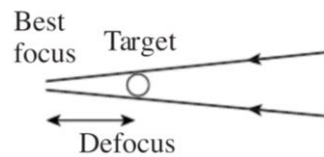


Figure 4. (a) Half of a cross-section of the proposed target. (b) A graph of the power (in W) against time of the optimized 2024 design. The blue line shows the actual power of the laser pulse. For the first two nanoseconds, the power is so low that it is barely visible. Then, there are two larger pulses, followed by a much larger pulse. This is done so that the target is gradually compressed, avoiding overheating. The green line shows the amount of power from the laser that was absorbed by the target, which was 85.6% integrated over the laser pulse. The red line is scattered power.

### 3. Optimization of Parameters

To achieve a uniform implosion, beams were moved in both the  $\theta$  and  $\varphi$  directions [Fig. 3]. Moving the rings'  $\theta$  angles towards the equator prevented the target from imploding in a “pancake” shape, as seen in Figure 2b. Furthermore, defocusing a beam widens the surface area of its impact, spreading out the energy from the beam [Fig. 5]. The best-focus beam shapes were taken from Ref. 6 and the defocused shapes were calculated following the method of Ref. 7. A variety of different parameter alterations were tested using the two-dimensional hydrodynamics simulation code, *Sage*<sup>8</sup>. Parameters were then altered based on the simulation results and the process was repeated. Earlier work [9] addressed the problem of optimizing direct drive on the LMJ, assuming that all 160 beams were available. However, since every other quad is absent from the framework in 2024, the work of Ref. 9 is inapplicable to the present problem. Another limitation of the earlier work is that it didn't attempt to optimize the azimuthal uniformity by adjusting the aimpoints in the  $\varphi$ -direction.



*Figure 5. The mechanics of defocusing. By moving the best focus away from the target, the surface area of the beam's impact is widened. (From Ref. 2)*

#### 4. Optimized Design for the LMJ at Half-Capacity

Table 1 depicts the positioning of the beams and the defocus used in order to optimize the LMJ direct drive configuration.

Optimal Parameters (80 Beams)				
	Upper Ring 1	Upper Ring 2	Lower Ring 1	Lower Ring 2
$\theta_0$	31.0°	35.5°	46.8°	51.3°
$\theta$	24.7°	55.0°	73.0°	85.0°
$\Delta\varphi$	$\pm 20.0^\circ$	$\pm 20.0^\circ$	$\pm 20.0^\circ$	$\pm 20.0^\circ$
<b>Defocus</b>	1.8 cm	1.8 cm	1.8 cm	1.8 cm

*Table 1. A table showing the optimized design for the LMJ in 2024. Upper ring 1 refers to the ring of aimpoints that corresponds to the upper beams of ring 1; the rest of the column names follow this same naming pattern. All of the  $\theta$  angles in the top hemisphere are reflected across the equator onto their corresponding angles in the bottom hemisphere. Beams in the same quad are moved by  $\Delta\varphi$  values (measured relative to the center of the quad) that are equal in magnitude to one another.  $\theta_0$  indicates the initial positioning of each ring on the target chamber. [Run 1056]*

The  $(\theta, \varphi)$  coordinates of the quad centers were taken from Ref. 6. The individual beam coordinates (including the Ring 1 and Ring 2  $\theta_0$  values) were calculated assuming nominal 40-cm-square beams with edges separated by 16.1 cm in the horizontal direction and 23.22 cm in the vertical direction, consistent with NIF values. Differences between these coordinates and actual LMJ coordinates are not expected to be significant as the parameters of the design given in Table 1 are all specified in terms of aimpoints. See Section 7.

To compensate for energy gaps created by the missing quads, it is important to change the  $\varphi$  angle of the aimpoints, moving them inwards towards the energy gap as shown in Figure 3. Furthermore, the  $\theta$  angles of most aimpoints were moved closer to the equator than

the initial angles  $\theta_0$  of the beams. This was done to avoid depositing too much energy at the poles of the target, thereby creating a more uniform implosion. Differently, upper ring 1 was not shifted towards the equator. Due to the shifts away from the poles of the other rings' beams, it was necessary to compensate for this loss of energy at the poles by repointing upper ring 1 closer to the poles of the target. Additionally, the implosion became more uniform as the beam defocus approached 1.8 cm. However, defocusing the beam farther caused too much energy to be lost and decreased the uniformity of the implosion.

The progress of the target's implosion is easily visible 7 ns after the laser is fired. At this point, the target has moved in an average of  $226 \mu\text{m}$  towards the target's center. As shown in Figure 6a, the target's implosion is very uniform, the average (*rms*) variation of distance being only  $2.06 \mu\text{m}$ . The average shell velocity in the  $\theta$ -direction is very uniform with the *rms* nonuniformity  $v\text{-rms-}\theta = 0.91\%$  [Fig 6b]. This was calculated by dividing the *rms* distance nonuniformity by the distance moved. Furthermore, Figure 6b provides a visual indication of the locations of the implosion's greatest nonuniformities. The maximum of the graph around  $90^\circ$  means that the target's radius was greater than average at the equator. This implies that less energy, on average, was received by the equator than by the rest of the target, compressing the target less. Oppositely, the radius diminishes at about  $75^\circ$  and  $105^\circ$ , which are the areas slightly removed from the equator. Future designs could work on decreasing this nonuniformity around the equator by shifting some beams slightly closer to the equator. There is also a noticeable spike in radius at one of the poles. However, this is most likely due to noise in *Sage* rather than from any true nonuniformity in the design.

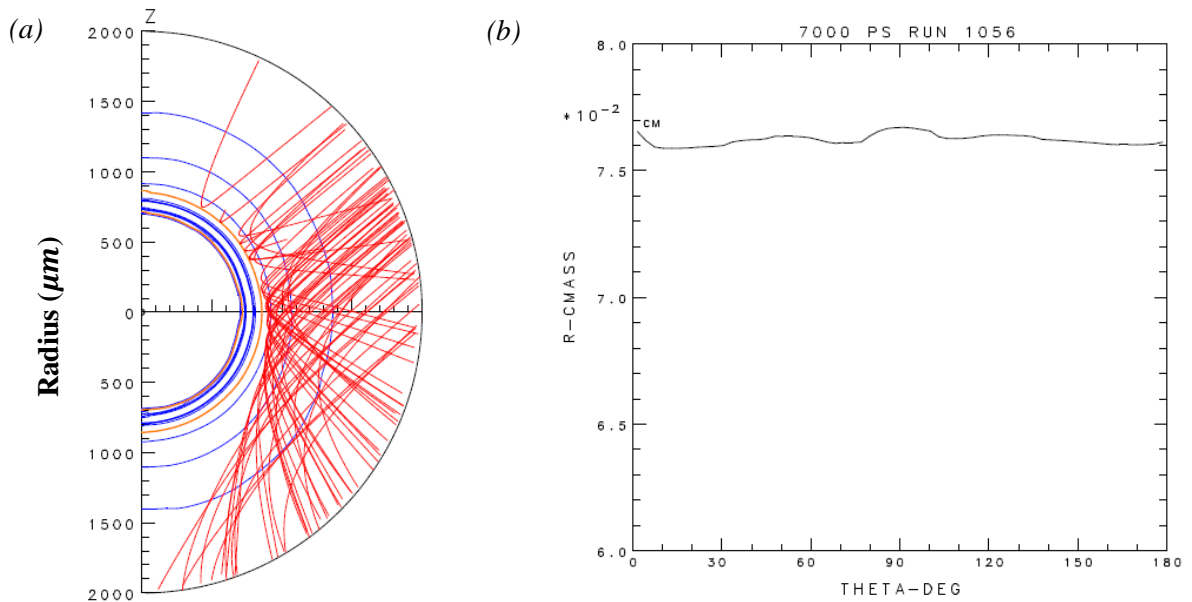


Figure 6. (a) A cross-section of the target 7 ns after the implosion began. When a ray is cut off, that implies that 99% of the ray's energy was absorbed by the target. The blue lines are electron density contours and the orange line represents the critical density, the highest density to which a laser ray can propagate. (b) The center-of-mass radius (in cm) as a function of  $\theta$  at 7 ns.

When the azimuthal direction is included in obtaining the  $v$ -rms, good overall uniformity of 2.03% is achieved [Fig. 7]. The center-of-mass radius varies between  $-11.73 \mu\text{m}$  and  $13.08 \mu\text{m}$  away from the average center-of-mass radius. Figure 7 provides information that aligns with the observations made from Figure 6b. The blue areas indicate where the center-of-mass radius is greater than average, in particular at the equator, while the red areas indicate a smaller radius. Furthermore, Figure 7 emphasizes the design's uniformity, as the radius differs from the average by less than one contour level at most areas on the target.

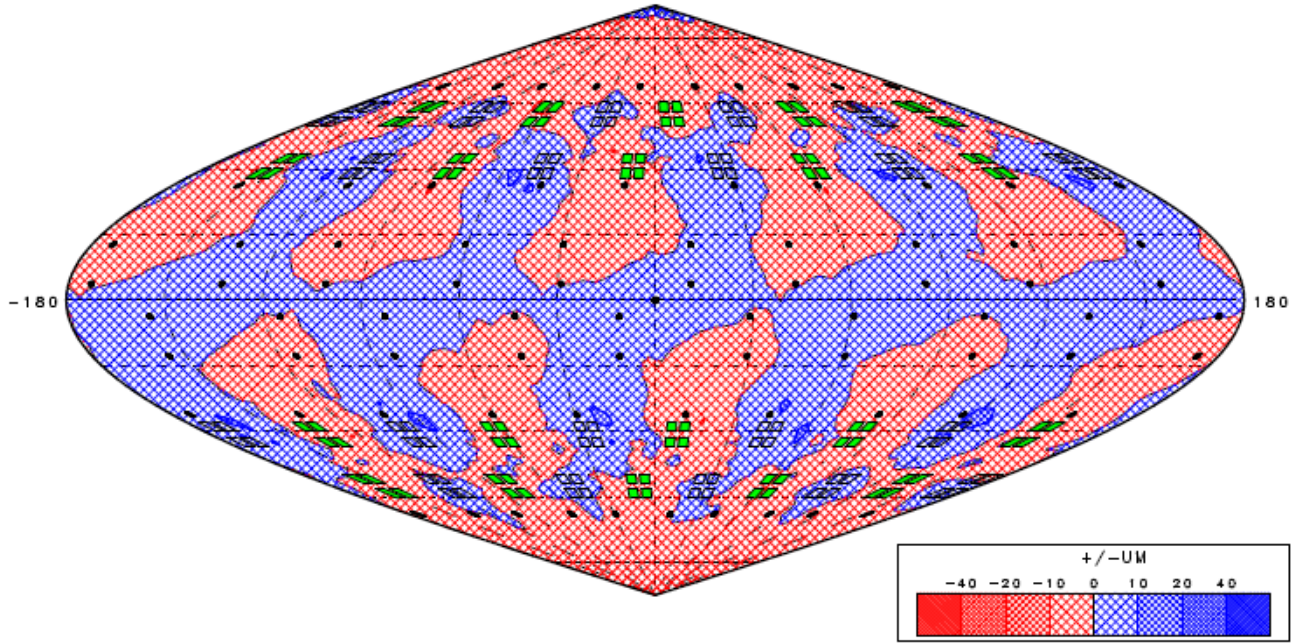


Figure 7. A contour plot of center-of-mass radius variations at 7 ns. [Run 1056]

From the overall  $v\text{-rms}$  of 2.03%, and the  $v\text{-rms-}\theta$  of 0.91%, the  $v\text{-rms-}\varphi$  may be calculated using the following formula:

$$v\text{-rms}^2 = v\text{-rms-}\theta^2 + v\text{-rms-}\varphi^2 \quad (1)$$

When the variables are replaced with their respective values, the following equation is evaluated:

$$2.03^2 = 0.91^2 + v\text{-rms-}\varphi^2 \quad (2)$$

showing that the  $rms$  variation in the  $\varphi$ -direction is  $v\text{-rms-}\varphi = 1.81\%$ . This is clearly larger than the  $v\text{-rms-}\theta$ , meaning that the nonuniformities lie more heavily in the  $\varphi$ -direction.

All tested deviations from the parameters of Table 1 caused an increase in the overall  $v\text{-rms}$ . For example, decreasing the Lower Ring 2  $\theta$  by  $0.2^\circ$  resulted in the  $v\text{-rms}$  increasing to 2.59%. Similarly, the  $v\text{-rms-}\theta$  increased to 1.90%. However, the  $v\text{-rms-}\varphi$  decreased to 1.75%, implying that moving the Lower Ring 2 aimpoints towards the poles would make the design more

longitudinally uniform, but less latitudinally uniform. This is the case for some, but not all other alterations of the parameters in Table 1. In some cases, beam shifts caused increases in both  $\theta$  and  $\varphi$   $v$ -rms. The results of calculating the various aspects of velocity uniformity were used in deciding which shifts or defocusing were needed to further optimize the design.

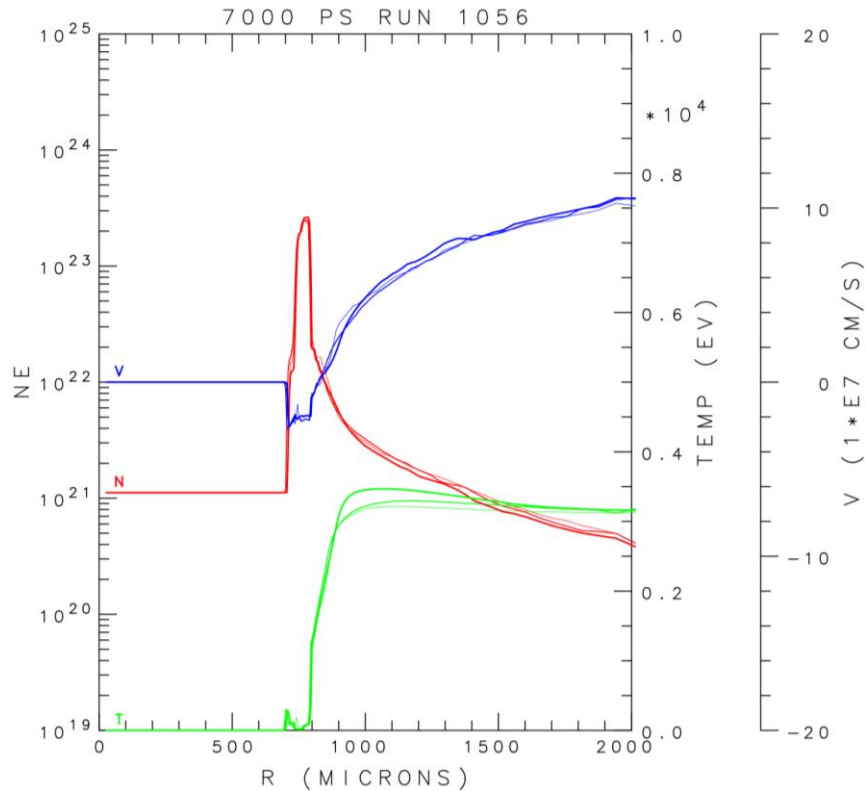


Figure 8. 1-D lineouts vs radius of electron temperature (eV, green), electron density (electrons/cc, red), and velocity in the radial direction (cm/s, blue). For each quantity, three lineouts are superposed at thetas of 1.45° (light), 45.00° (medium), and 88.55° (heavy). The almost exact overlays demonstrate the high uniformity.

Figure 8 provides further proof of this design’s high levels of uniformity. It shows curves depicting the electron temperature, electron density, and radial velocity of the target during the implosion. The electron temperature is higher on the outside of the target but falls off to a lower value inside the target. As energy is conducted into the target, the outer layer of the shell is heated and ablates off the target. The second curve, electron density, shows low density at time

0, everywhere except for where the initial shell is. As plasma ablates and moves outwards, the opposing force moves the shell inwards. In the center, the density of the undisturbed gas remains a constant  $10^{21}/\text{cc}$ . Furthermore, the third curve, velocity, is positive in almost all places, showing a movement outwards. The shell's negative velocity depicts its inward motion. Since the three different curves taken from  $1.45^\circ$ ,  $45.00^\circ$ , and  $88.55^\circ$  in the  $\theta$ -direction are shown to overlay each other almost exactly, it can be assumed that the electron temperature, electron density, and velocity of the target remain uniform during the implosion.

Moreover, the uniformity is even better than what one might initially think; the main goal is to match the density profiles (showing that the shell moves with the same speed), which this run does exceedingly well. Additionally, in order to perform polar direct drive, the temperature at  $\theta = 90^\circ$  must be slightly higher, as seen in the electron temperature profiles. This is because the energy deposited near the equator is deposited further from critical (the maximum density to which the laser can propagate), and therefore drives the shell less effectively. Overall, the results of Figure 8 confirm the high uniformity of this design.

## 5. Optimized Design for the LMJ at Full Capacity

When the LMJ is fully developed, it will need a different beam configuration in order to facilitate a uniform implosion. Those parameters are shown in Table 2.

<b>Optimal Parameters (160 Beams)</b>				
	<b>Upper Ring 1</b>	<b>Upper Ring 2</b>	<b>Lower Ring 1</b>	<b>Lower Ring 2</b>
<b><math>\theta_0</math></b>	31.0°	35.5°	46.8°	51.3°
<b><math>\theta</math></b>	24.5°	55.0°	73.0°	86.0°
<b><math>\Delta\varphi</math></b>	$\pm 5.5^\circ$	$\pm 5.5^\circ$	$\pm 5.5^\circ$	$\pm 5.5^\circ$
<b>Defocus</b>	1.8 cm	1.8 cm	1.8 cm	1.8 cm

*Table 2. A table showing the optimized design for the LMJ at full capacity. [Run 1093]*

While there are some minor changes in the  $\theta$ -direction in comparison with Table 1, the most significant alteration comes in the  $\varphi$ -direction. The  $\Delta\varphi$  decreases from  $\pm 20.0^\circ$  to  $\pm 5.5^\circ$  [Table 2]. This is due to the difference in configuration of the LMJ at half capacity, compared to the LMJ at full capacity. When the LMJ is at full capacity, there will be twice as many beams active, meaning that the energy gaps that plagued the half capacity facility will not be present. Therefore, there is less of a need to strongly alter each beam's  $\Delta\varphi$ .

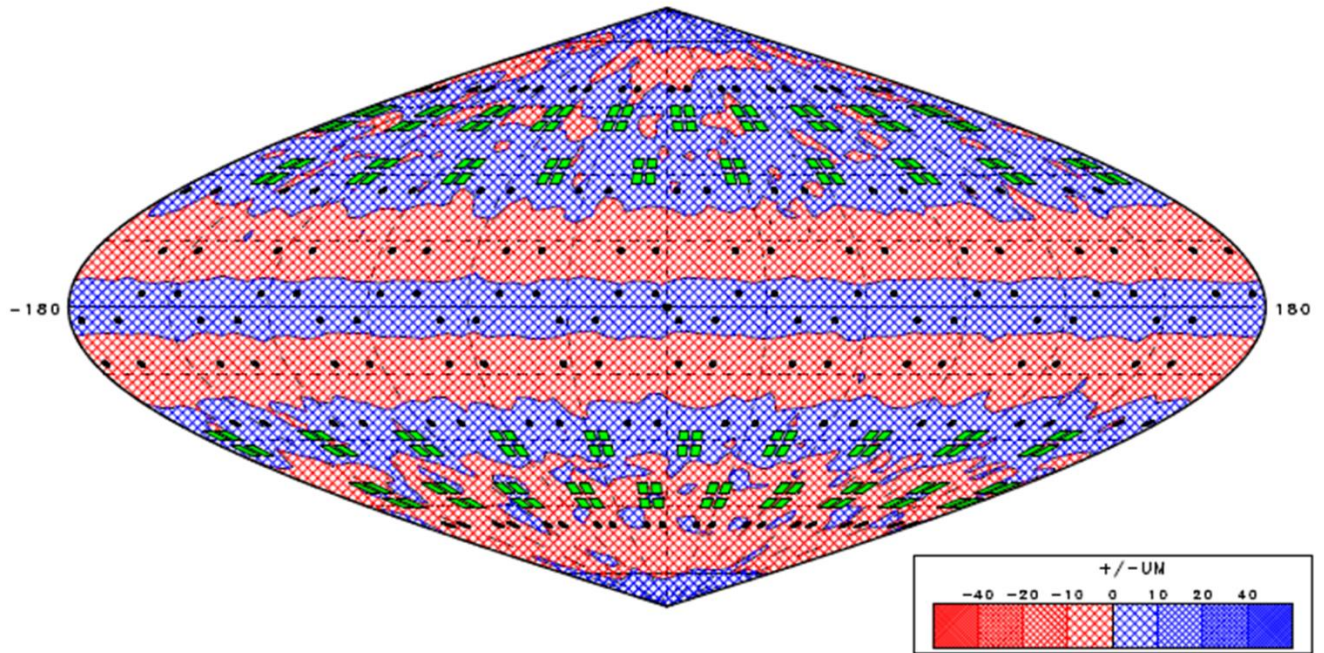


Figure 10. A contour plot of center-of-mass radius variations at 7 ns when the LMJ is at full capacity. [Run 1093]

Even better uniformity is achieved when all beams are active, with the energy of each beam halved so that the same total energy is delivered to the target. The overall  $v$ -rms is 0.98%, which is a significant decrease from 2.03% [Fig.10]. Furthermore, the  $v$ -rms in the  $\theta$ -direction is 0.82% and the  $v$ -rms in the  $\varphi$ -direction is 0.53%. In contrast with the half capacity optimized configuration, the full capacity configuration is more uniform in the  $\varphi$ -direction than in the  $\theta$ -direction. Moreover, the center-of-mass radius varies between  $-5.19 \mu\text{m}$  and  $5.89 \mu\text{m}$  around the average radius, which is about half the range of the half capacity configuration. Likewise, in terms of absorption, the full capacity design was more efficient, absorbing 87.3% (rather than 85.6%) of the energy from the beams.

## 6. Conclusion

This work proposes beam configurations that will optimize the uniformity of a direct drive implosion on the LMJ, which is designed for indirect drive implosions. The 2-D hydrodynamics code *Sage* was used to simulate different configurations when optimizing each solution. Good uniformity was achieved by adjusting the aimpoints and defocuses of the beams. When the LMJ is at half capacity, it may reach uniformity levels of 2.03%, and when it is at full capacity, it can attain improved uniformity levels of 0.98%.

## 7. Note Added

Since the simulations reported here were carried out, the actual individual LMJ beam coordinates were made available [10]. The coordinates used for the work reported here, estimated as described in Section 4, turned out to be very close to the actual coordinates. The  $\theta$  values were all within  $0.1^\circ$  and the  $\varphi$  values were all within  $0.5^\circ$ , so no modifications are necessary to the designs given here. Indeed, when the half-capacity design of Section 4 (Run 1056) was rerun with the actual coordinates, the uniformity changed by an insignificant amount (from 2.03% to 1.98%) as did the absorption (from 85.6% to 85.2%).

## 8. Acknowledgements

I would like to thank Dr. Craxton for his invaluable guidance and support on this project. He made this internship a wonderful opportunity for growth. Furthermore, I would like to

thank the entire LLE community for providing this opportunity to both myself and future students.

## 9. References

1. “Pursuing Fusion Ignition,” National Ignition Facility & Photon Science (2021).
2. A. M. Cok, “Development of Polar Direct Drive Designs for Initial NIF Targets,” Laboratory for Laser Energetics High School Summer Research Program (2006).
3. W. Wang, “Development of a Beam Configuration for the SG4 Laser to Support both Direct and Indirect Drive,” Laboratory for Laser Energetics High School Summer Research Program (2020).
4. P.A. Norreys et al., LMJ-PETAL Facility : Letter of Intent, “Measuring 1-D like behaviour of a 240 kJ low convergence ratio hydrodynamically equivalent ICF capsule,” (2020).
5. R.W. Paddock, private communication (May 2021).
6. LMJ-PETAL Users Guide, Version 2.0, CEA, France.
7. A. M. Cok et al., “Polar-drive designs for optimizing neutron yields on the National Ignition Facility,” Phys. Plasmas 15, 082705 (2008).
8. R. S. Craxton and R. L. McCrory, “Hydrodynamics of Thermal Self-Focusing in Laser Plasmas,” J. Appl. Physics. 56, 108 (1984).
9. L. M. Mitchell, “Exploration of the Feasibility of Polar Drive on the LMJ,” Laboratory for Laser Energetics High School Summer Research Program (2009).
10. B. Canaud, private communication (November 2022).